PHYSICS

Exciton control in a room temperature bulk semiconductor with coherent strain pulses

Edoardo Baldini[1]*[†], Adriel Dominguez[2], Tania Palmieri[1], Oliviero Cannelli[1],
Angel Rubio[2,3,4], Pascal Ruello[5], Majed Chergui[1†]

Controlling the excitonic optical properties of room temperature semiconductors using time-dependent perturbations is key to future optoelectronic applications. The optical Stark effect in bulk and low-dimensional materials has recently shown exciton shifts below 20 meV. Here, we demonstrate dynamical tuning of the exciton properties by photoinduced coherent acoustic phonons in the cheap and abundant wide-gap semiconductor anatase titanium dioxide (TiO_2) in single crystalline form. The giant coupling between the excitons and the photoinduced strain pulses yields a room temperature exciton shift of 30 to 50 meV and a marked modulation of its oscillator strength. An advanced ab initio treatment of the exciton-phonon interaction fully accounts for these results, and shows that the deformation potential coupling underlies the generation and detection of the giant acoustic phonon modulations.

INTRODUCTION

New perspectives in the field of excitonics have recently developed from the discovery of strongly bound excitons that persist at room temperature (RT) in several semiconductors, including organics (1), hybrid organic-inorganic metal halide perovskites (2, 3), transition metal dichalcogenides (4), and transition metal oxides (5–7). Despite their different origin, excitons in these classes of materials are strongly coupled to the lattice degrees of freedom. Because excitons can be viewed as quanta of electronic excitation energy traveling in the periodic crystal lattice, their motion is influenced by the fluctuating potential field due to lattice vibrations. On the fundamental aspect, exciton-phonon coupling is an intriguing type of boson-boson interaction that results in phenomena such as exciton self-trapping, spectral-weight transfers to phonon sidebands, and Stokes-shifted emissions (8). On the practical side, identifying the specific modes (acoustic or optical) that couple strongly to the excitons paves the way for the control of the exciton properties (e.g., binding energy, oscillator strength, and lifetime) through the tailored application of strain, pressure, or photoexcitation.

Experimentally, the microscopic details of the exciton in the phonon field can be addressed via absorption and photoluminescence spectroscopy, because the shape and width of the optical spectra directly reflect the coupling of the exciton to the lattice vibrations (9). However, the information offered by these methods is mediated over all the coupled phonon modes. This calls for more advanced techniques that can yield information on the exciton-phonon coupling for specific lattice modes of interest to allow, in return, the phonon-selective control of the exciton properties. A powerful tool relies on setting a particular phonon mode out of equilibrium and monitoring the impact of the ionic motion on the exciton spectral features (10, 11).
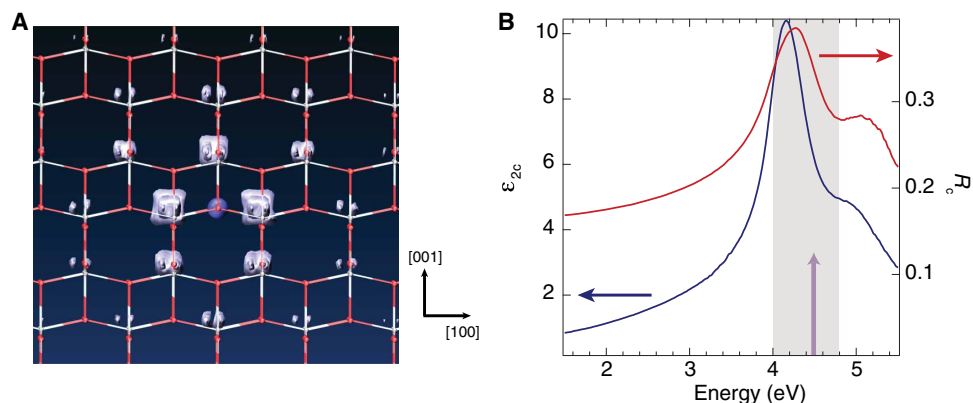
This is possible by time- and energy-resolved optical spectroscopy, in which a system is first excited by an ultrashort laser pulse and the changes in the optical properties are tracked with a delayed optical probe covering the exciton line shape. This approach also opens the door to the high-speed control of the exciton properties via ultrafast light excitation. So far, the coherent manipulation of excitons through the photoinduced ionic motion has led to exciton shifts as large as 10 meV in semiconductor nanostructures and only at very low temperatures (12, 13). At RT, shifts of <1 meV have only been reached in quantum dots (14), where the exciton-phonon coupling is enhanced by the low dimensionality. This poses serious limitations for the design of efficient acousto-excitonic devices.

An alternative strategy involves the use of bulk semiconductors that are known to host strongly bound excitonic resonances at RT and simultaneously show strong electron-phonon coupling. An ideal material system is the anatase polymorph of TiO_2, which is a superior candidate for several applications, ranging from photocatalysis and transparent conductive substrates to photovoltaics and sensors. Its optical absorption spectrum is dominated by strongly bound excitons (binding energy $E_B > 100$ meV) with an intermediate Wannier-Mott and Frenkel character (7). Light polarized in the (001) crystallographic plane can resonantly activate the lowest-energy (a-axis) exciton, which is characterized by a two-dimensional wave function in the three-dimensional crystal lattice. In contrast, resonant excitation with a polarization state along the [001] axis results in the formation of the highest-energy (c-axis) exciton, which has a fairly localized wave function in all three directions, with an average Bohr radius of 0.7 to 2 nm (Fig. 1A). These excitons are very robust against external perturbations, persisting at RT and at high photodoped carrier densities, as well as in defect-rich nanoparticles and mesoporous films (7, 15, 16). There exists a moderately strong coupling between the electronic degrees of freedom that build up the exciton states and the polar optical modes of the lattice via the Fröhlich interaction (17). However, the study of the direct coupling between the excitonic states and the acoustic modes is still in its infancy. Recently, we demonstrated that near-to-mid ultraviolet (UV) femtosecond laser pulses can coherently excite acoustic phonons that are confined in anatase TiO_2 nanoparticles at RT, leading to a marked modulation in the oscillator strength of the material's a-axis exciton (18). Although such an effect points toward a significant coupling between excitons and acoustic phonons in anatase

Fig. 1. Characterization of the *c*-axis exciton in anatase TiO₂. (**A**) Calculated wave function of the *c*-axis exciton. The isosurface representation shows the electronic configuration when the hole of the considered excitonic pair is localized close to one oxygen atom. The colored region represents the excitonic squared modulus wave function. (**B**) Imaginary part of the dielectric function (blue curve) and reflectivity (red curve) of anatase TiO₂ measured at RT, with the electric field polarized along the *c* axis. The experimental data are obtained from (*7*), as measured by spectroscopic ellipsometry. The pump photon energy of 4.50 eV used for the pump-probe experiment is indicated by the violet arrow, and the probed region is highlighted as a gray shaded area.

TiO₂, its theoretical understanding was hindered by the averaging effect due to the random distribution of the nanoparticles and the fact that the confined mechanical vibrations of these nanosized objects depend on the boundary conditions. Using a single crystal of anatase TiO₂ provides a more direct and precise way of probing the acoustic phonon/exciton coupling matrix elements. Moreover, future acousto-optic and acousto-excitonic applications would benefit from the coherent control of excitons through the use of propagating strain pulses in bulk substrates, rather than confined modes in nanosized particles. Hence, extraordinary RT acoustic effects in the case of anatase TiO₂ single crystals are highly desirable.

Here, using ultrafast broadband spectroscopy in the near-to-mid UV, we reveal the signature of propagating coherent acoustic phonons that couple directly to the *c*-axis exciton of anatase TiO₂ single crystals. In our experiments, we take advantage of the extraordinarily high ($N \sim 10^{21}$ cm^{-3}) carrier densities that this material can support, compared to other systems, to produce a giant modulation of the reflectivity amplitude by means of the coherent phonons, indicating efficient generation/detection of the acoustic modes. Furthermore, the strong exciton-phonon coupling leads to a 30-meV shift of the exciton peak, which is the largest ever reported in solid materials under a time-dependent perturbation. We rationalize our findings within the framework of many-body perturbation theory, providing a complete quantitative treatment of such a strong exciton-phonon interaction.

RESULTS

High-quality anatase TiO₂ single crystals were grown by a chemical vapor transport method and oriented via Laue diffraction to expose a (010) surface to the incoming radiation. Figure 1B shows the imaginary part (ε_{2c}) of the dielectric function of these single crystals at RT with light polarized parallel to the *c* axis (blue trace), along with the material reflectivity (R_c) as derived from the dielectric function (red trace). These spectra are obtained from our spectroscopic ellipsometry data in (*7*), which provided an extensive steady-state characterization of the single crystals used for the experiments here. The ε_{2c} trace features a sharp peak at 4.15 eV, which is due to the excitonic transition (*7*). In equilibrium, the broadening of the excitonic resonance is governed by the electronic lifetime of the electron-hole states

involved in the exciton formation (in TiO₂, this depends only on nonradiative recombination channels) and by the scattering events that the excitons undergo immediately after their creation by light absorption. The latter comprise exciton-phonon and exciton-impurity collisions. A weaker charge excitation lies around 5.00 eV and is ascribed to a resonant interband transition within the continuum. Consistently, R_c presents similar features at 4.26 and 5.15 eV, respectively.

In our nonequilibrium experiment, we excite the crystal with an ultrashort laser pulse polarized along the *c* axis. Its photon energy of 4.50 eV (violet arrow in Fig. 1B) lies above the exciton peak, which leads to a nonresonant excitation of uncorrelated electron-hole pairs. We set the photoexcited carrier density to $N \sim 3.5 \times 10^{20}$ cm^{-3} at the threshold between the linear and the nonlinear regime for anatase TiO₂ so as to maximize the light-induced acoustic effects (*16*). Subsequently, we monitor the relative changes in the material *c*-axis reflectivity ($\Delta R/R$) using a white light continuum probe over the spectral range of 4.00 to 4.80 eV. This unique capability allows us to span the entire exciton profile (gray shaded area in Fig. 1B). The time resolution of the experiments is set on purpose at 700 fs to isolate the pure contribution of slow acoustic transients and filter out any additional effect due to faster Raman-active optical phonons (*19*) that can mask the acousto-excitonic coupling. More details are found in Materials and Methods.

Figure 2A displays the color-coded map of $\Delta R/R$ as a function of the probe photon energy during the first 10 ps of pump-probe delay. We observe a negative $\Delta R/R$ response, which persists over the temporal window of our experiment (~1 ns). This feature corresponds to the *c*-axis exciton resonance, and it is primarily modified by the effect of the photoexcited carrier density (*7*). On top of this electronic incoherent background, the exciton resonance experiences a pronounced sinusoidal modulation during the first 6 ps, which is particularly evident around 4.10 eV. To visualize how the exciton line shape is modified during the sinusoidal modulation, in Fig. 2 (B and C), we present the $\Delta R/R$ spectra at representative time delays in the first 6 ps. Figure 2B shows the full measured response between 4.00 and 4.80 eV, while Fig. 2C zooms into the spectral range of 4.20 to 4.35 eV, with the spectra vertically shifted for clarity. The $\Delta R/R$ spectrum at 0.5 ps (red curve) displays the exciton response before the sinusoidal modulation; thus, it identifies the response of the exciton resonance
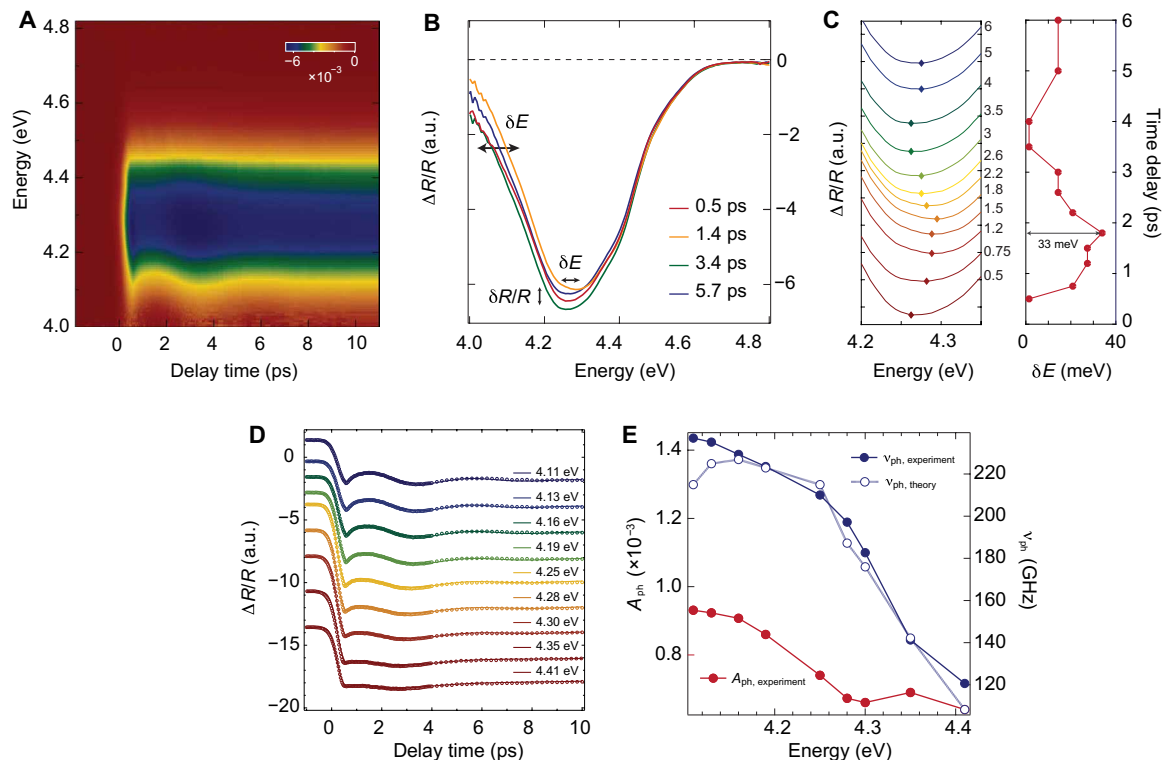
Fig. 2. Ultrafast broadband UV spectroscopy data. (**A**) Color-coded map of $\Delta R/R$ at RT as a function of probe photon energy and time delay between pump and probe. Both pump and probe beams are polarized along the material c axis. The pump photon energy is 4.50 eV. (**B**) Transient spectra of $\Delta R/R$ for different time delays during the coherent acoustic phonon evolution. The exciton peak undergoes a $\delta E = 30$-meV variation in energy and a $\delta R/R \sim 5\%$ change in intensity. The low-energy tail of the exciton also reacts to the modulation, shifting by 50 meV. a.u., arbitrary units. (**C**) Zoom-in of the transient spectra of $\Delta R/R$ for different time delays during the first 6 ps of the response. The time-dependent variation of the exciton peak energy is also shown. (**D**) Temporal traces of $\Delta R/R$ for different probe photon energies (dotted lines), as indicated in the label. The solid lines are fits to the experimental data. (**E**) Probe photon energy dependence of the amplitude (A_{ph}) and frequency (ν_{ph}) of the coherent oscillations with a comparison between experiment and theory.

to the excitation of uncorrelated electron-hole pairs. The shape of the differential signal suggests that only the oscillator strength of the whole exciton peak changes due to phase-space filling (i.e., exciton bleach in the corresponding transient absorption spectrum). The peak energy in this curve matches that of the static reflectivity, and the absence of any first derivative– or second derivative–like response suggests that no shift or broadening of the resonance has occurred. Hence, the spectrum at 0.5 ps can be considered as a reliable reference to quantify the effects of the subsequent sinusoidal oscillation on the exciton line shape. These effects are evident in the spectra between 0.75 and 6 ps, in terms of a pronounced variation of the exciton peak energy ($\delta E \sim 30$ meV), amplitude ($\delta R/R \sim 5\%$ of the total signal at the exciton peak), and asymmetry (shift of 50 meV in the exciton low-energy tail). Because of the static linewidth of the exciton resonance (~300 meV), the coherent modulation-induced signal remains negative at all time delays. Complementary insights into the ultrafast response are offered by the temporal traces, which are shown in Fig. 2D at representative photon energies. They feature a resolution-limited rise, followed by a large-amplitude coherent response on top of the flat background caused by phase-space filling. The modulation is strongly damped, vanishing after two periods. Its frequency is much lower than that of optical phonons in anatase TiO$_2$ (*19*), and it varies with the probe photon energy. To retrieve the photon energy dependence of the modulation frequency, we perform a standard global fit of the temporal traces by simultaneously fitting

nine traces in the range of 4.10 to 4.42 eV while fixing the same time constants. An accurate fit can only be obtained using a multi-exponential background function and a damped sinusoidal term convoluted with our instrument response function. The fitted curves are shown in Fig. 2D as solid lines on top of the experimental traces. The dependence of the modulation amplitude (red trace) and frequency (blue trace) on the probe photon energy is plotted in Fig. 2E and reflects the behavior of the raw data. We observe that the amplitude peaks around 4.11 eV, i.e., on the low-energy wing of the exciton resonance. Furthermore, the modulation frequency varies with the probe photon energy, which is not expected in the case of coherent optical phonons. This observable supports the idea that the modulations are due to longitudinal acoustic phonons propagating along the [010] axis of the anatase TiO$_2$ single crystal.

Light-induced coherent acoustic phonons in bulk solids and nanostructures have been a subject of numerous studies, especially with all-optical (*10*, *20*) and extreme UV/x-ray (*21–23*) pump-probe methods. In all-optical experiments, a femtosecond pump pulse excites the sample out of equilibrium and leads, through different electron-phonon and phonon-phonon coupling mechanisms, to the emission of coherent acoustic phonons. In bulk solids, these coherent wave packets are generated by the pump pulse in the subsurface region and propagate toward the bulk of the material at the speed of sound. A delayed probe laser pulse can detect their signature only during the time that these phonons are present in the optically

accessible sample region (while propagating from the subsurface to the bulk). This, in turn, determines the apparent damping of the coherent oscillations in the temporal traces.

So far, in all-optical pump-probe experiments, coherent acoustic phonon phenomena have been investigated with photon energy lying in the material's transparency region or in the proximity of its interband transitions (10). However, the interplay between the propagating acoustic modes and excitonic collective states in bulk solids is still unexplored. This framework holds promise especially in the case of materials with a strong exciton-phonon coupling, as the coherent strain field can lead to marked effects on the exciton bound states. Consistent with this idea, we note that the modulation depth of the exciton oscillator strength provided by the coherent acoustic phonons in bulk anatase TiO_2 is among the largest ever experimentally observed. Comparable signals have only been reported in semiconductor nanostructures (24, 25), where the electron-phonon coupling is strongly enhanced by quantum confinement. We also underline that the detected exciton shift is the highest ever reached in solid materials under the influence of a time-dependent perturbation, as summarized in Table 1. Although this exciton peak shift is one order of magnitude smaller than the linewidth of the resonance, it translates into a selective change in the exciton E_B while leaving the lifetime (which controls the linewidth of the spectral feature) almost intact. In the past, comparable or larger RT exciton shifts have been found only in low-dimensional semiconductors under the application of static stimuli, such as electric fields (26, 27) and uniaxial strains of a few percent (28, 29). This marked modulation of the exciton line shape cannot be solely related to the high carrier density photoexcited in the material ($\sim 10^{20}$ cm^{-3}), because other highly excited bulk insulators hosting strongly bound excitons do not even display coherent acoustic phonon phenomena at similar excitation densities (30). In contrast, the observed dynamical renormalization of the RT excitonic properties in bulk anatase TiO_2 is a consequence of the strong exciton-acoustic phonon coupling in this material, which calls for a complete theoretical description.

To this aim, in the following, we reveal the details of this boson-boson interaction by means of many-body perturbation theory. Such an advanced ab initio treatment of the exciton-acoustic phonon coupling in bulk solids has never been explored before, as previous computational works analyzed this fundamental interaction only at a standard density functional theory (DFT) level (31). The present analysis shows that the deformation potential (DP) coupling lies at the origin of the observed effects in anatase TiO_2. First, we underline that the observed coherent acoustic phonons cannot be generated via an electro-acoustic effect, as anatase TiO_2 is not a piezoelectric

material. Moreover, we can also rule out the involvement of a surface polarization (due to an inhomogeneous distribution of oxygen vacancies at the material surface) in the generation of the coherent strain pulse. The screening of a built-in surface field upon photoexcitation would lead to the narrowing of the exciton line shape over time (32), which is not observed in our case.

As a second step, we evaluate the efficiency of the DP coupling by providing a quantitative description of the coherent acoustic phonon transient reflectivity signal ($\delta R/R$). As well known from the literature, if the probe photon energy lies within the bandgap of an insulator, the detection mechanism can be interpreted in terms of the conventional Brillouin scattering process (33), in which only the real part of the material's refractive index is modulated and the phonon frequency linearly depends on the probe light wave vector $\mathbf{k}$ inside the material ($\nu_{ph} = \mathbf{k} \, \nu/2\pi$, where ν is the sound velocity). In contrast, when the material is opaque to the probe photon energy (like in our experiments), a more general expression has to be considered for the detection process, which includes the contribution of imaginary parts of both the refractive index and the photoelastic coefficient. This is accounted for by the general perturbative approach developed by Thomsen et al. (34), in which the strain-induced change in reflectivity reads

$$\frac{\delta R}{R} = 2\Re \left\{ \frac{4i \mathbf{k}_0 \tilde{n}}{1 - \tilde{n}^2} \frac{d\tilde{n}}{d\eta} \int_0^\infty \eta(z,t) e^{2i\mathbf{k}_0 \tilde{n} z} \, dz \right\} \quad (1)$$

where $\Re$ denotes the real part, $z = 0$ defines the crystal surface, $\mathbf{k}_0$ is the probe light wave vector in vacuum, and $\tilde{n} = n_1 + i n_2$ is the complex refractive index. This expression is governed by the time-dependent spatial overlap integral between the longitudinal coherent strain field, $\eta(z, t)$, and the electric field of the backscattered probe light. The exciton-phonon coupling strength is embodied by the complex photoelastic coefficient $d\tilde{n}/d\eta$, which is linked to the DP matrix element. In the linear regime of photoelasticity (i.e., for a small strain of the order of $10^{-5}/10^{-4}$), this quantity is assumed to be independent of the strain, thus leading to an opposite but equivalent shift in magnitude of the material optical spectrum under the application of compressive or tensile stress. To evaluate Eq. 1, the photoelastic coefficient is needed. Because the photoelastic coefficient in the near-to-mid UV is not known, we rely on state-of-the-art band structure calculations. Although the description of the optical response becomes challenging in the presence of strong excitonic correlations, in (7, 35), we showed that many-body perturbation theory provides a very accurate model of the electronic and optical properties of TiO_2 single crystals. Here, we extend this approach to the case of strained anatase TiO_2 and extract the fundamental

Table 1. Exciton shifts in different materials under distinct time-dependent perturbations.

Material	Dimensionality	Perturbation	Temperature	Exciton shift	Reference
$Zn_{1-x}Cd_xSe$	Quantum wells	Pulsed light field	10 K	4 meV	(45)
WS_2, WSe_2	Monolayer	Pulsed light field	295 K	10–18 meV	(38, 39)
$CH_3NH_3PbI_3$	Bulk	Pulsed light field	295 K	10 meV	(40)
GaAs/AlGaAs	Heterostructure	Pulsed strain field	1.8 K	1 meV	(12)
ZnSe/ZnMgSSe	Quantum wells	Pulsed strain field	1.8 K	10 meV	(13)
CdSe	Quantum dots	Pulsed strain field	295 K	<1 meV	(14)
Anatase TiO_2	Bulk	Pulsed strain field	295 K	30–50 meV	This work

electron-phonon matrix elements that are relevant for both the generation [photoinduced strain $\eta(z, t)$] and the detection (photoelastic coefficient $d\tilde{n}/d\eta$) mechanisms. More details about the theoretical methods are given in Materials and Methods.

We calculate the single-particle excitation spectrum of the material at the GW level while applying a 0.2% deformation of the unit cell along the [010] axis. This deformation is artificially introduced to mimic the photoinduced strain propagating in the crystal under our experimental conditions and to study its effects on the single-particle electronic structure. In a second step, we compute the optical spectrum in the presence of many-body electron-hole correlations by solving the Bethe-Salpeter equation (BSE) and studying how the excitons are renormalized by the macroscopic strain field. We remark that our theoretical analysis is performed in the case of a pristine TiO$_2$ crystal, taking into account only direct optical transitions and neglecting the additional screening induced by free carriers and the presence of indirect (phonon- or impurity-assisted) transitions. Although the latter effects are not expected to modify our conclusions [as discussed in (7)], they could be responsible for some of the remaining discrepancies between theory and experiment. The GW approach allows us to refine the values of the DPs obtained by standard DFT (36). Our estimate of the DPs experienced by the lowest states in the valence (d_h) and conduction band (d_e) yields $d_h = -0.066$ eV/GPa and $d_e = -0.096$ eV/GPa. The negative sign of the DPs suggests that the photoinduced stress is compressive in nature. This allows us to evaluate the efficiency of the DP mechanism in comparison to the other dominant generation process in nonmagnetic and non-piezoelectric materials, which is the thermoelastic mechanism (phonon pressure). From our analysis (see section S2), we conclude that the DP mechanism provides a contribution ~30 times larger than that of thermoelasticity.

Thereafter, we compute the dielectric function and the reflectivity in the case of the unstrained unit cell and in the presence of a tensile/compressive strain along the [010] axis (fig. S3 and Fig. 3, A and B). We find that the exciton peak strongly reacts to the strain field, undergoing a marked renormalization of its energy and a pronounced modulation of its intensity. The peak energy shift ($\delta E = 30$ meV) and intensity change ($\delta R/R = 3.5\%$) in the reflectivity show an excellent match with the experimental data. Moreover, the observed strain dependence of the exciton peak suggests that the photoelastic coefficients $dn_1/d\eta$ and $dn_2/d\eta$ are not symmetric upon application of compressive or tensile strain (see fig. S4). Specifically, in the presence of a tensile strain, the exciton peak undergoes a larger shift to the red; in contrast, upon the application of a compressive strain, the exciton displays higher resistance to blue shift. This aspect indicates that the c-axis exciton in anatase TiO$_2$ undergoes an anomalous renormalization due to the nonlinearity of the photoelastic coefficients. So far, most of the nonlinearities in ultrafast acoustics come from nonlinear acoustic properties illustrated by the observations of solitons (13) or shock waves (37). In contrast, our data suggest that under the present experimental conditions, the system is driven into a nonperturbative regime because the photoinduced strain is large and the damped sinusoidal acoustic signal predicted by the Thomsen model may be distorted. The new physics that is highlighted here is that of nonlinear exciton-acoustic phonon coupling phenomena in strongly interacting semiconductors, which is still a rather unexplored territory in condensed matter research.

To simplify the modeling of our data within the perturbative regime, we calculate the photoelastic coefficients using the central finite dif-

ferences method (Fig. 3C). Large values are found in the vicinity of the exciton resonance, indicating that the electron–phonon coupling is effective only in this photon energy range. Last, we evaluate Eq. 1 using the parameters computed above. We consider that the photoinduced DP stress is produced within the skin depth of the pump field ($\xi = \lambda/4\pi n_2 \sim 12$ nm). Because the crystal is semi-infinite, the resulting photoinduced strain pulse is assumed to be bipolar, with $\eta(z, t) = -\eta_0 \, \text{sign}(z - vt)e^{-|z-vt|/\xi}$. This assumption is reasonable, as during the time range over which the phenomena are observed (0 to 10 ps), the acoustic pulse cannot develop an N-wave or form acoustic solitons. On the basis of the computed DPs and elastic properties (a bulk modulus $B = 181$ GPa), the photoinduced strain along the [010] direction is $\eta_0 = (d_e + d_h)BN/\rho_0 v^2 \sim 10^{-3}$ (ρ_0 is the mass density). The final calculation is performed with the computed photoelastic coefficients of Fig. 3C, whereas the conventional approach of ultrafast acoustics (which makes use of the steady-state linear optical data) provides a poor agreement in the presence of such a high value of photoinduced strain (see section S3). We underline that these photoelastic coefficients reach values that are two orders of magnitude larger than those of GaAs and are thus responsible for the giant modulation depth of the exciton oscillator strength (see section S3). Our refined model yields damped sinusoidal functions that are shown in Fig. 3D and compared with the experimental traces. We observe that the coherent response is well reproduced and the calculated frequencies ($\nu_{\text{ph,th}}$; Fig. 2E) are in excellent agreement with the experimental ones. Small deviations in the modulation amplitude (by a factor of $0.6 \div 1.2$) and damping are caused by the distortion that the signal undergoes beyond the perturbative regime. Some of the traces were multiplied by -1 to match the experimental curves, implying that our model does not reproduce the phase of the modulation over the whole probed range. The phase depends on the ratio between the real and imaginary part of the photoelastic coefficient, which are calculated here with the method of the central differences to mimic the perturbative regime of the Thomsen model. Thus, the disagreement between the phase observed in our experimental data and the one predicted by the Thomsen model shows the limit of our approach at this stage. Considering the above limiting points, the overall agreement between our data and the model is very good, and the ab initio calculations provide relevant values of physical parameters to successfully reproduce the amplitude of the transient reflectivity signal. We underline that the optical spectra calculated with the random phase approximation on top of the GW results do not provide realistic signals (7), leading to much smaller photoelastic coefficients than the experimental ones (see section S4). This highlights the importance of solving the BSE to address the impact of the lattice motion on the excitonic states, a hitherto unexplored treatment, which opens new perspectives for the accurate prediction and design of tailored exciton-phonon coupling schemes. Future extensions of the Thomsen model to the nonperturbative regime and in the presence of exciton nonlinearities will reveal the complex structure of the electron-phonon coupling in strongly interacting materials such as anatase TiO$_2$.

DISCUSSION

In this work, the combination of state-of-the-art ultrafast broadband UV spectroscopy and many-body perturbation theory calculations has allowed us to elucidate the details of the coupling between excitons and coherent acoustic phonons in the technologically relevant anatase TiO$_2$. Efficient generation and detection of coherent acoustic
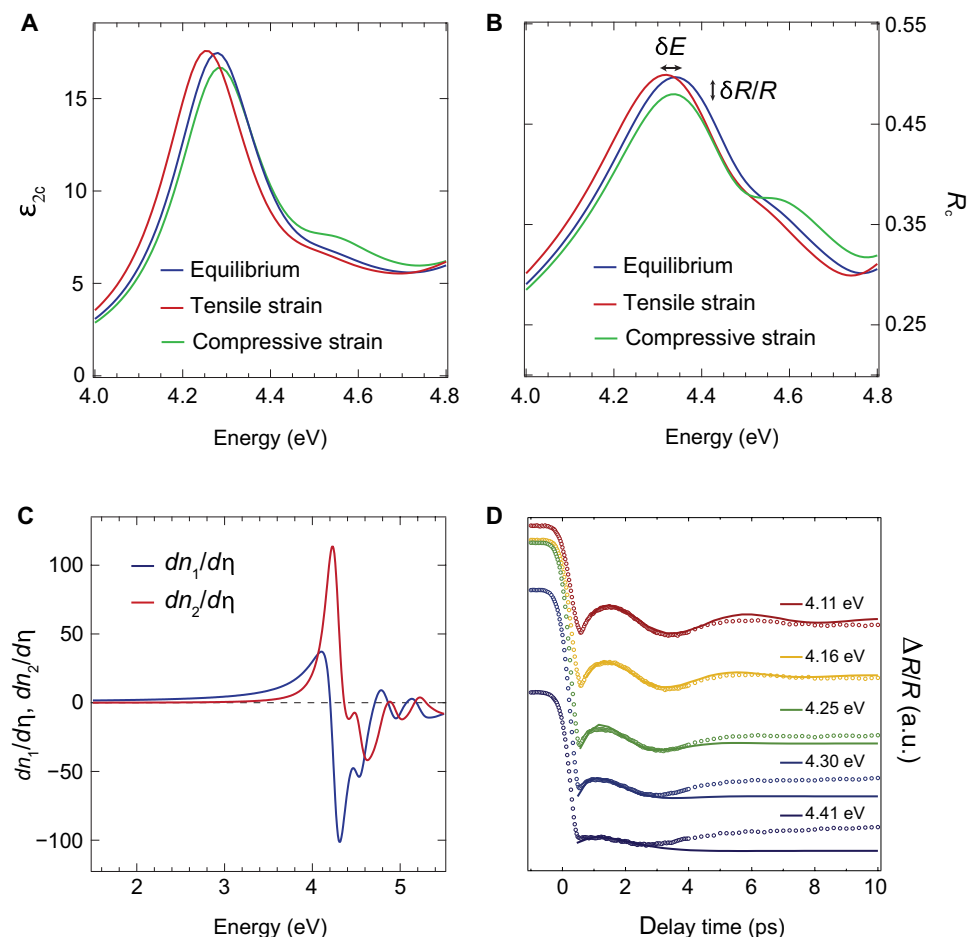
Fig. 3. Many-body perturbation theory calculations and simulated acoustic response. (**A**) Calculated imaginary part of the dielectric function in the BSE-GW scheme for the equilibrium unit cell (blue curve) and in the presence of a 0.2% tensile (red curve) and compressive (green curve) strain. (**B**) Calculated reflectivity in the BSE-GW scheme for the equilibrium unit cell (blue curve) and in the presence of tensile (red curve) and compressive (green curve) strain. (**C**) Calculated real (blue curve) and imaginary (red curve) parts of the photoelastic coefficient. (**D**) Simulated transient acoustic response at different probe photon energies (solid lines), as indicated in the labels. The dotted lines are the experimental data.

phonons in the range of 100 to 200 GHz are observed at RT in the vicinity of an exciton resonance. During the time in which the two collective excitations interact, the coherent strain pulse affects the relevant exciton properties. The duration of this interaction is determined by the spatial extension of the coherent acoustic phonon pulse. In TiO_2, the spatial localization of the coherent strain (which propagates at a speed of 9100 m/s) is determined by the optical penetration depth of the deep-UV pump (~15 nm). Because the coherent acoustic phonons that are emitted in the near surface area are reflected at the free surface (to ensure the mechanical boundary condition of zero stress at a free surface), the total spatial extension of the acoustic field is then twice this value, i.e., 30 nm. As a consequence, the interaction time between acoustic phonons and excitons can be estimated around 4 ps in the current experiment. The main result of this interaction is the exceptional exciton band tuning of 30 to 50 meV with a moderate strain value.

This finding recovers a peculiar importance when compared to the coherent manipulation of excitons via the light field itself within the framework of the optical Stark effect, which so far has produced RT exciton shifts over the visible range of 10 to 20 meV in transition metal dichalcogenides (*38*, *39*) and 2 meV in hybrid perovskites (*40*).

Thus, our observation opens intriguing perspectives for near-to-mid UV acousto-optics and acousto-excitonics, in which the additional electronic contribution to the exciton renormalization can be suppressed by engineering a source of coherent acoustic phonons (such as a metallic film) on top of an anatase TiO_2 crystal. Our study demonstrates a method that can be easily extended to other classes of bulk insulators with bound excitons and a relatively strong electron-phonon coupling. In the case of bulk band semiconductors, a prototypical example is offered by the perovskite titanates [E_B = 220 meV in $SrTiO_3$ (*6*)], which are characterized by very anharmonic lattice potentials. Another avenue that can be explored is the lattice-mediated coherent control of excitons living in a correlated electronic environment, i.e., in bulk Mott-Hubbard and charge-transfer insulators (e.g., NiO). Besides being governed by strong electronic correlations, this class of solids is well known to have a prominent coupling between the electronic degrees of freedom and a variety of bosonic collective modes (e.g., phonons, magnons, and orbitons). Thus, the control of Mott-Hubbard excitons with coherent strain pulses appears as a promising frontier in condensed matter physics and could lead to the periodic modulation of other fundamental interactions, such as the on-site Coulomb and exchange coupling. Last, the use of coherent

acoustic phonons is expected to cause marked changes in the properties of two-dimensional excitons hosted by monolayer semiconductors, such as transition metal dichalcogenides (e.g., MoS_2 and WS_2) (4) or trihalides (e.g., CrI_3) (41). For these reasons and in analogy to the growing field of active plasmonics (42), we believe that active excitonics, in which the excitonic transport can be selectively modulated at high speeds by tailored opto-acoustic stimuli, offers new perspectives for the development of novel devices.

MATERIALS AND METHODS

Single-crystal growth and characterization
High-quality single crystals of anatase TiO_2 were produced by a chemical transport method from anatase powder and NH_4Cl as transport agent, similar to the procedure described in (7). In detail, 0.5 g of high-purity anatase powder was sealed in a 3-mm-thick, 2-cm-large, and 20-cm-long quartz ampoule together with 150 mg of NH_4Cl, previously dried at 60°C under dynamic vacuum for one night, and 400 mbar of electronic grade HCl. The ampoules were placed in a horizontal tubular two-zone furnace and heated very slowly to 740°C at the source and to 610°C at the deposition zone. After 2 weeks, millimeter-sized crystals with a bipyramidal shape were collected and cut into rectangular bars (typically 0.8 mm × 0.6 mm × 0.15 mm). The doping level was determined via angle-resolved photoemission spectroscopy or transport measurements to be $n = 2 \times 10^{19}$ cm^{-3}.

Ultrafast broadband near-to-mid UV spectroscopy
The ultrafast optical experiments were performed using a novel setup of tunable near-to-mid UV pump and broadband UV probe, described in detail in (7). A 20-kHz Ti:sapphire regenerative amplifier (KMLabs, Halcyon + Wyvern 500), providing pulses at 1.55 eV, with 0.6-mJ energy and around 50-fs duration, pumped a noncollinear optical parametric amplifier (NOPA) (TOPAS-white, Light Conversion) to generate sub–90 fs visible pulses (range, 1.77 to 2.30 eV). The typical output energy per pulse was 13 μJ. Around 60% of the output of the NOPA was used to generate the narrowband pump pulses. The visible beam, after passing through a chopper, operating at 10 kHz and phase-locked to the laser system, was focused onto a 2-mm-thick β-barium borate crystal for nonlinear frequency doubling. The pump photon energy was controlled by the rotation of the crystal around the ordinary axis and could be tuned in a spectral range up to ~0.9 eV (~60 nm) wide. For our purpose, the pump photon energy was set at 4.50 eV to selectively perturb the spectral region above the c-axis excitonic peak of anatase TiO_2. The typical pump bandwidth was 0.02 eV (1.5 nm), and the maximum excitation energy was about 120 nJ. The pump power was recorded on a shot-to-shot basis by a calibrated photodiode for each pump photon energy, allowing the normalization of the data for the pump power. The remaining NOPA output was used to generate the broadband UV probe pulses with ~1.3-eV (~100 nm) bandwidth through an achromatic doubling scheme.

To study the anatase TiO_2 single crystals, the setup was used in the reflection geometry. The specimens were mounted on a rotating sample holder to explore the transient reflectivity ($\Delta R/R$) along the desired crystalline axis. Pump and probe pulses, which have the same polarization, were focused onto the sample, where they were spatially and temporally overlapped. The typical spot size of the pump and the probe were 100 and 40 μm full width at half maximum,

respectively, resulting in a homogeneous illumination of the probed region. The portion of the probe beam reflected by the surface of the crystal was detected, and the time evolution of the difference in the UV probe reflection with and without the pump pulse was reconstructed. After the sample, the reflected probe was focused in a multimode optical fiber (100 μm), coupled to the entrance slit of a 0.25-m imaging spectrograph (Chromex 250is). The beam was dispersed by a holographic grating (150 g/mm) and imaged onto a multichannel detector consisting of a 512-pixel CMOS (complementary metal-oxide semiconductor) linear sensor (pixel size, 12.5 μm × 250 μm; Hamamatsu S11105) with up to 50-MHz pixel readout, so the maximum readout rate per spectrum (almost 100 kHz) allowed us to perform shot-to-shot detection easily. All the experiments were performed at RT.

Many-body perturbation theory calculations
Many-body perturbation theory at the level of the GW and the BSE (43) was used to compute the band structure and the dielectric response of bulk anatase TiO_2. The GW and BSE calculations were performed on top of eigenvalues and eigenfunctions obtained from DFT. We used the planewave pseudopotential implementation of DFT as provided by the package Quantum ESPRESSO. For the GW and BSE calculations, we used the BerkeleyGW package (41). The DFT calculations were performed using the generalized gradient approximation as in the Perdew-Burke-Ernzerhof (PBE) scheme for the exchange-correlation functional. The Ti norm-conserving pseudopotential was generated in the Rappe-Rabe-Kaxiras-Joannopoulos scheme, including semicore 3s and 3p states. While standard structural and electronic quantities are already converged in DFT with an energy cutoff of 90 Ry, the energy cutoff used here was raised to 160 Ry to properly include the high number of bands necessary to reach convergence for the many-body evaluated properties. Bulk anatase TiO_2 was modeled on a body-centered tetragonal lattice containing two Ti atoms and four O atoms (primitive cell) with lattice parameters (optimized at the PBE level) $a = b = 3.79$ Å and $c = 9.66$ Å. The experimental lattice constants at RT are $a = b = 3.78$ Å and $c = 9.51$ Å. Scaling these parameters to zero temperature via a linear extrapolation of the temperature dependence of the lattice constant at high temperature, appearing in (44), yields $a = b = 3.78$ Å and $c = 9.49$ Å.

The ground-state electronic density is properly described with a coarse $4 \times 4 \times 4$ k-point grid for sampling of the Brillouin zone. The GW quasiparticle corrections to the DFT eigenvalues were performed at the one-shot level of theory (G_0W_0). For the computation of the polarizability and inverse dielectric matrices in BerkeleyGW, we used a total of 2474 conduction bands (CBs) and G-vectors with kinetic energies up to 46 Ry, whereas the self-energy operator was computed using 2472 unoccupied bands and a G-vector cutoff energy of 46 and 160 Ry for the screened and bare Coulomb matrices, respectively. The coarse $4 \times 4 \times 4$ k-point grid sampling is sufficient for the description of the quasiparticle corrections, while a high number of bands are mandatory to get a proper description of screening effects and many-body corrections. The electronic band structure was finally obtained by interpolating GW corrections on top of a more refined DFT calculation with a $16 \times 16 \times 16$ grid. The fully converged BSE results shown in the main text were obtained with BerkeleyGW. We used a shifted grid with up to $16 \times 16 \times 16$ k-points (4096 irreducible k-points). The six lowest CBs and six topmost valence bands (VBs) were included to solve the excitonic Hamiltonian. Spin-polarized calculations were performed to highlight possible dark excitons due to

triplet excitations, but no measurable differences with respect to the spin-restricted results were obtained. More details are provided in (*7*).

To estimate the role of the electron-acoustic phonon coupling in the electronic and optical properties of anatase TiO_2, we performed frozen phonon DFT + GW + BSE calculations by applying a strain of 0.2% along the [010] crystallographic direction. The results of these calculations are shown in Fig. 3 (A to C).

SUPPLEMENTARY MATERIALS

Supplementary material for this article is available at http://advances.sciencemag.org/cgi/content/full/5/11/eaax2937/DC1

Section S1. Global fit analysis
Section S2. Generation mechanism
Section S3. Phenomenological description of the observed exciton renormalization
Section S4. Perturbative model for coherent acoustic phonons
Section S5. Additional many-body perturbation theory calculations
Fig. S1. Traditional approach of ultrafast acoustics applied to anatase TiO_2.
Fig. S2. Simulation of the transient acoustic signal.
Fig. S3. Many-body perturbation theory calculations on the strained unit cell.
Fig. S4. Calculation of the photoelastic coefficients.
Fig. S5. Comparison between the RPA-GW and BSE-GW results.
References (*46*, *47*)

REFERENCES AND NOTES

1. W. Brütting, *Introduction to the Physics of Organic Semiconductors* (Wiley Online Library, 2006).
2. H. Kunugita, T. Hashimoto, Y. Kiyota, Y. Udagawa, Y. Takeoka, Y. Nakamura, J. Sano, T. Matsushita, T. Kondo, T. Miyasaka, K. Ema, Excitonic feature in hybrid perovskite $CH_3NH_3PbBr_3$ single crystals. *Chem. Lett.* **44**, 852–854 (2015).
3. L. M. Herz, Charge-carrier dynamics in organic-inorganic metal halide perovskites. *Annu. Rev. Phys. Chem.* **67**, 65–89 (2016).
4. J. R. Schaibley, H. Yu, G. Clark, P. Rivera, J. S. Ross, K. L. Seyler, W. Yao, X. Xu, Valleytronics in 2D materials. *Nat. Rev. Mater.* **1**, 16055 (2016).
5. C. Klingshirn, R. Hauschild, J. Fallert, H. Kalt, Room-temperature stimulated emission of ZnO: Alternatives to excitonic lasing. *Phys. Rev. B* **75**, 115203 (2007).
6. P. K. Gogoi, L. Sponza, D. Schmidt, T. C. Asmara, C. Diao, J. C. Lim, S. M. Poh, S. Kimura, P. E. Trevisanutto, V. Olevano, A. Rusydi, Anomalous excitons and screenings unveiling strong electronic correlations in $SrTi_{1−x}Nb_xO_3$ (0≤x≤0.005). *Phys. Rev. B* **92**, 035119 (2015).
7. E. Baldini, L. Chiodo, A. Dominguez, M. Palummo, S. Moser, M. Yazdi-Rizi, G. Auböck, B. P. P. Mallett, H. Berger, A. Magrez, C. Bernhard, M. Grioni, A. Rubio, M. Chergui, Strongly bound excitons in anatase TiO_2 single crystals and nanoparticles. *Nat. Commun.* **8**, 13 (2017).
8. Y. Toyozawa, *Optical Processes in Solids* (Cambridge Univ. Press, 2003).
9. K. S. Song, R. T. Williams, *Self-Trapped Excitons* (Springer Science & Business Media, 2013).
10. P. Ruello, V. E. Gusev, Physical mechanisms of coherent acoustic phonons generation by ultrafast laser action. *Ultrasonics* **56**, 21–35 (2015).
11. A. Mann, E. Baldini, A. Tramontana, E. Pomjakushina, K. Conder, C. Arrell, F. Van Mourik, J. Lorenzana, F. Carbone, Probing the electron-phonon interaction in correlated systems with coherent lattice fluctuation spectroscopy. *Phys. Rev. B* **92**, 035147 (2015).
12. A. V. Akimov, A. V. Scherbakov, D. R. Yakovlev, C. T. Foxon, M. Bayer, Ultrafast band-gap shift induced by a strain pulse in semiconductor heterostructures. *Phys. Rev. Lett.* **97**, 037401 (2006).
13. A. V. Scherbakov, P. J. S. Van Capel, A. V. Akimov, J. I. Dijkhuis, D. R. Yakovlev, T. Berstermann, M. Bayer, Chirping of an optical transition by an ultrafast acoustic soliton train in a semiconductor quantum well. *Phys. Rev. Lett.* **99**, 057402 (2007).
14. D. M. Sagar, R. R. Cooney, S. L. Sewall, E. A. Dias, M. M. Barsan, I. S. Butler, P. Kambhampati, Size dependent, state-resolved studies of exciton-phonon couplings in strongly confined semiconductor quantum dots. *Phys. Rev. B* **77**, 235321 (2008).
15. E. Baldini, T. Palmieri, T. Rossi, M. Oppermann, E. Pomarico, G. Auböck, M. Chergui, Interfacial electron injection probed by a substrate-specific excitonic signature. *J. Am. Chem. Soc.* **139**, 11584–11589 (2017).
16. E. Baldini, T. Palmieri, E. Pomarico, G. Auböck, M. Chergui, Clocking the ultrafast electron cooling in anatase titanium dioxide nanoparticles. *ACS Photonics* **5**, 1241–1249 (2018).
17. S. Moser, L. Moreschini, J. Jacimovic, O. S. Barisic, H. Berger, A. Magrez, Y. J. Chang, K. S. Kim, A. Bostwick, E. Rotenberg, L. Forro, M. Grioni, Tunable polaronic conduction in anatase TiO_2. *Phys. Rev. Lett.* **110**, 196403 (2013).
18. E. Baldini, T. Palmieri, A. Dominguez, P. Ruello, A. Rubio, M. Chergui, Phonon-driven selective modulation of exciton oscillator strengths in anatase TiO_2 nanoparticles. *Nano Lett.* **18**, 5007–5014 (2018).
19. K. Ishioka, H. Petek, Raman generation of coherent phonons of anatase and rutile TiO_2 photoexcited at fundamental absorption edges. *Phys. Rev. B* **86**, 205201 (2012).
20. J. A. Rogers, A. A. Maznev, M. J. Banet, K. A. Nelson, Optical generation and characterization of acoustic waves in thin films: Fundamentals and applications. *Annu. Rev. Mater. Sci.* **30**, 117–157 (2000).
21. C. Rose-Petruck, R. Jimenez, T. Guo, A. Cavalleri, C. W. Siders, F. Rksi, J. A. Squier, B. C. Walker, K. R. Wilson, C. P. J. Barty, Picosecond-milliångström lattice dynamics measured by ultrafast x-ray diffraction. *Nature* **398**, 310–312 (1999).
22. D. A. Reis, M. F. DeCamp, P. H. Bucksbaum, R. Clarke, E. Dufresne, M. Hertlein, R. Merlin, R. Falcone, H. Kapteyn, M. M. Murnane, J. Larsson, T. Missalla, J. S. Wark, Probing impulsive strain propagation with x-ray pulses. *Phys. Rev. Lett.* **86**, 3072–3075 (2001).
23. R. M. Karl Jr., G. F. Mancini, J. L. Knobloch, T. D. Frazer, J. N. Hernandez-Charpak, B. Abad, D. F. Gardner, E. R. Shanblatt, M. Tanksalvala, C. L. Porter, C. S. Bevis, D. E. Adams, H. C. Kapteyn, M. M. Murnane, Full-field imaging of thermal and acoustic dynamics in an individual nanostructure using tabletop high harmonic beams. *Sci. Adv.* **4**, eaau4295 (2018).
24. C.-K. Sun, J.-C. Liang, X.-Y. Yu, Coherent acoustic phonon oscillations in semiconductor multiple quantum wells with piezoelectric fields. *Phys. Rev. Lett.* **84**, 179–182 (2000).
25. A. Devos, F. Poinsotte, J. Groenen, O. Dehaese, N. Bertru, A. Ponchet, Strong generation of coherent acoustic phonons in semiconductor quantum dots. *Phys. Rev. Lett.* **98**, 207402 (2007).
26. D. A. B. Miller, D. S. Chemla, T. C. Damen, A. C. Gossard, W. Wiegmann, T. H. Wood, C. A. Burrus, Band-edge electroabsorption in quantum well structures: The quantum-confined Stark effect. *Phys. Rev. Lett.* **53**, 2173–2176 (1984).
27. Y.-H. Kuo, Y. K. Lee, Y. Ge, S. Ren, J. E. Roth, T. I. Kamins, D. A. B. Miller, J. S. Harris, Strong quantum-confined Stark effect in germanium quantum-well structures on silicon. *Nature* **437**, 1334–1336 (2005).
28. J. O. Island, A. Kuc, E. H. Diependaal, R. Bratschitsch, H. S. van der Zant, T. Heine, A. Castellanos-Gomez, Precise and reversible band gap tuning in single-layer MoS_2 by uniaxial strain. *Nanoscale* **8**, 2589–2593 (2016).
29. O. B. Aslan, M. Deng, T. F. Heinz, Strain tuning of excitons in monolayer WSe_2. *Phys. Rev. B* **98**, 115308 (2018).
30. S. Richter, O. Herrfurth, S. Espinoza, M. Rebarz, M. Kloz, J. A. Leveillee, A. Schleife, S. Zollner, M. Grundmann, J. Andreasson, R. Schmidt-Grund, Ultrafast dynamics of hot charge carriers in an oxide semiconductor probed by femtosecond spectroscopic ellipsometry. arXiv:1902.05832 [cond-mat.mtrl-sci] (15 February 2019).
31. D. Rossi, L. E. Camacho-Forero, G. Ramos-Sánchez, J. H. Han, J. Cheon, P. Balbuena, D. H. Son, Anisotropic electron-phonon coupling in colloidal layered TiS_2 nanodiscs observed via coherent acoustic phonons. *J. Phys. Chem. C* **119**, 7436–7442 (2015).
32. A. N. Cartwright, D. S. McCallum, T. F. Boggess, A. L. Smirl, T. S. Moise, L. J. Guido, R. C. Barker, B. S. Wherrett, Magnitude, origin, and evolution of piezoelectric optical nonlinearities in strained [111] B InGaAs/GaAs quantum wells. *J. Appl. Phys.* **73**, 7767–7774 (1993).
33. L. Brillouin, Diffusion de la lumière et des rayons x par un corps transparent homogène. Influence de l'agitation thermique. *Ann. Phys.* **17**, 88–122 (1922).
34. C. Thomsen, H. T. Grahn, H. J. Maris, J. Tauc, Surface generation and detection of phonons by picosecond light pulses. *Phys. Rev. B* **34**, 4129–4138 (1986).
35. E. Baldini, A. Dominguez, L. Chiodo, E. Sheveleva, M. Yazdi-Rizi, C. Bernhard, A. Rubio, M. Chergui, Anomalous anisotropic exciton temperature dependence in rutile TiO_2. *Phys. Rev. B* **96**, 041204 (2017).
36. W.-J. Yin, S. Chen, J.-H. Yang, X.-G. Gong, Y. Yan, S.-H. Wei, Effective band gap narrowing of anatase TiO_2 by strain along a soft crystal direction. *Appl. Phys. Lett.* **96**, 221901 (2010).
37. A. Bojahr, M. Herzog, D. Schick, I. Vrejoiu, M. Bargheer, Calibrated real-time detection of nonlinearly propagating strain waves. *Phys. Rev. B* **86**, 144306 (2012).
38. J. Kim, X. Hong, C. Jin, S.-F. Shi, C.-Y. S. Chang, M.-H. Chiu, L.-J. Li, F. Wang, Ultrafast generation of pseudo-magnetic field for valley excitons in WSe_2 monolayers. *Science* **346**, 1205–1208 (2014).
39. E. J. Sie, J. W. McIver, Y. H. Lee, L. Fu, J. Kong, N. Gedik, Valley-selective optical Stark effect in monolayer WS_2. *Nat. Mater.* **14**, 290–294 (2015).
40. Y. Yang, M. Yang, K. Zhu, J. C. Johnson, J. J. Berry, J. Van De Lagemaat, M. C. Beard, Large polarization-dependent exciton optical Stark effect in lead iodide perovskites. *Nat. Commun.* **7**, 12613 (2016).
41. M. Wu, Z. Li, T. Cao, S. Louie, Physical origin of giant excitonic and magneto-optical responses in two-dimensional ferromagnetic insulators. *Nat. Commun.* **10**, 2371 (2019).
42. K. F. MacDonald, Z. L. Sámson, M. I. Stockman, N. I. Zheludev, Ultrafast active plasmonics. *Nat. Photonics* **3**, 55–58 (2009).
43. J. Deslippe, G. Samsonidze, D. A. Strubbe, M. Jain, M. L. Cohen, S. G. Louie, BerkeleyGW: A massively parallel computer package for the calculation of the quasiparticle and optical properties of materials and nanostructures. *Comput. Phys. Commun.* **183**, 1269–1289 (2012).

44. K. V. K. Rao, S. V. N. Naidu, L. Iyengar, Thermal expansion of rutile and anatase. *J. Am. Ceram. Soc.* **53**, 124–126 (1970).

45. J. A. Gupta, R. Knobel, N. Samarth, D. D. Awschalom, Ultrafast manipulation of electron spin coherence. *Science* **292**, 2458–2461 (2001).

46. O. B. Wright, B. Perrin, O. Matsuda, V. E. Gusev, Ultrafast carrier diffusion in gallium arsenide probed with picosecond acoustic pulses. *Phys. Rev. B* **64**, 081202 (2001).

47. E. Shojaee, M. R. Mohammadizadeh, First-principles elastic and thermal properties of TiO$_2$: A phonon approach. *J. Phys. Condens. Matter* **22**, 015401 (2010).

Citation: E. Baldini, A. Dominguez, T. Palmieri, O. Cannelli, A. Rubio, P. Ruello, M. Chergui, Exciton control in a room temperature bulk semiconductor with coherent strain pulses. *Sci. Adv.* **5**, eaax2937 (2019).

Science Advances

Exciton control in a room temperature bulk semiconductor with coherent strain pulses

Edoardo Baldini, Adriel Dominguez, Tania Palmieri, Oliviero Cannelli, Angel Rubio, Pascal Ruello and Majed Chergui

ARTICLE TOOLS	http://advances.sciencemag.org/content/5/11/eaax2937
SUPPLEMENTARY MATERIALS	http://advances.sciencemag.org/content/suppl/2019/11/21/5.11.eaax2937.DC1
REFERENCES	This article cites 43 articles, 3 of which you can access for free http://advances.sciencemag.org/content/5/11/eaax2937#BIBL
PERMISSIONS	http://www.sciencemag.org/help/reprints-and-permissions

Use of this article is subject to the Terms of Service